

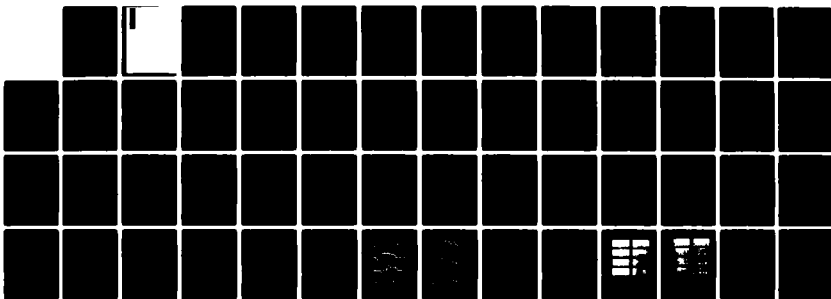
AD-A136 410

TIME DEPENDENT COMPRESSIBLE SIMULATIONS OF SHEAR FLOWS: 1/1
TESTS OF OUTFLOW..(U) NAVAL RESEARCH LAB WASHINGTON DC
J BORIS ET AL. 12 DEC 83 NRL-MR-5249 SBI-AD-E000 556

UNCLASSIFIED

F/G 20/4

NL



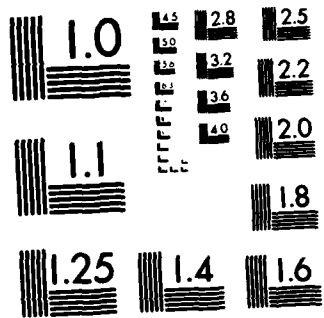
END

DATE

FILMED

84

DTIC



MICROCOPY RESOLUTION TEST CHART
NATIONAL BUREAU OF STANDARDS-1963-A

AD A136410

20. ABSTRACT (Continued)

outflow boundary conditions is discussed and detailed benchmarks are given for two problems: a round jet flowing into a quiescent background gas and a diaphragm in a barrel. Finally, two calculations are described: one of a round jet surrounded by a slower co-flowing gas and the other of a splitter plate.

CONTENTS

I. INTRODUCTION 1

II. BACKGROUND 3

III. THE NUMERICAL MODEL 8

IV. OUTFLOW BOUNDARY CONDITIONS 10

V. TEST OF THE OUTFLOW ALGORITHM: DIAPHRAGM IN A BARREL 13

 1. The Test Problem 13

 2. The Outflow Algorithm 15

 3. Results of the Calculations 16

VI. TEST OF THE OUTFLOW ALGORITHM: CYLINDRICAL GAS JET 19

 1. The Test Problem 19

 2. The Outflow Algorithm 20

 3. Results of the Calculations 21

 4. Discussion 23

VII. GAS JET AND SPLITTER PLATE SIMULATIONS 24

 1. The Splitter Plate 24

 2. The Gas Jet 27

VIII. DISCUSSION AND SUMMARY 31

ACKNOWLEDGMENTS 32

REFERENCES 49

DTIC
COPY
INSPECTED
3

SEARCHED
SERIALIZED
INDEXED
FILED

APR 1 1963

AD-1

TIME DEPENDENT, COMPRESSIBLE SIMULATIONS OF SHEAR FLOWS: TESTS OF OUTFLOW BOUNDARY CONDITIONS

I. INTRODUCTION

This paper describes recent numerical simulations performed at NRL of shear flows transitioning to turbulence, and, in particular, the development and evolution of coherent structures. There are two aspects of this problem which are addressed in this report. The first is developing and testing the model that was used in these studies. In particular, we are concerned with the treatment of inflow and outflow boundary conditions suitable for both compressible and incompressible flows. The second aspect is using this model to describe shear flows.

The first problem, developing the proper computational tools, has been the major goal of the last year's work and is discussed in Sections III through VI. The numerical model we are using now is a restructured version of the FAST2D computer code. This incorporates the Flux-Corrected Transport (FCT) continuity equation algorithm (Boris, 1976b; Boris and Book, 1976) which has been tested extensively for shock, detonation, and beam-generated turbulence calculations (e.g., Book et al., 1980, Oran et al., 1982; Picone and Boris, 1983). Since the algorithm is explicit in its present form, the code is particularly efficient for studying flows that move at a substantial fraction of the speed of sound in the material. Using time step splitting techniques, we couple FCT to algorithms for the other physical processes we want to represent. In Section III below we describe the general features of the code. In Section IV, V, and VI we describe tests of the new outflow boundary conditions.

The second aspect, application of the model, is the goal of the upcoming research. We have used the model to simulate time dependent flows in two configurations, the splitter plate and the round jet, for which substantial

Manuscript approved October 28, 1983.

data exist on the transition to turbulence. At the end of this paper, in Section VII, we describe some preliminary results and their implications.

II. BACKGROUND

The development and structure of turbulent flows is the focus of intense study. We now know that flows which previously were thought to be totally chaotic and statistical in nature are dominated by the persistence of relatively large structures. These coherent structures were previously ignored since their existence was masked or de-emphasized by experimental averaging techniques. The classical description of turbulence and the mechanisms responsible for its development are now considered deficient in their explanations of these transient but organized and persistent structures.

The classical description of turbulence evolved from the observed behavior of fluid flows as a function of Reynolds number. Many flows exhibit a series of sudden transitions to new flow patterns as the Reynolds number is increased. Each transition results in an increasingly complicated flow, and at high Reynolds number the flows become irregular and appear chaotic in both space and time. The transitions to the succession of flow patterns may be caused by a sequence of fluid instabilities, each of which breaks some symmetry in the previously stable flow pattern and introduces some new scale in the flow pattern (Liepmann, 1979). The transition to a purely chaotic flow was postulated to occur through an infinite succession of instabilities, each contributing to the increasing frequency content of the flow (Landau and Lifshitz, 1959).

Several experimental observations have seriously eroded confidence in the completeness of such a turbulence model for physical flows. First, although laboratory created grid turbulence comes close, no flow has yet been shown to exhibit pure, homogeneous isotropic turbulence in the classical sense. Such a state is really a limiting condition. Further, since coherent

structures exist on the larger scales, it is reasonable to assume the existence of similar structure on all scales larger than the dissipation scale. Second, the transition to turbulence does not occur through an infinite succession of instabilities, but after the appearance of relatively few instabilities, typically three or four. This has led to the postulate of a theoretical connection between strange attractor theory and transition to turbulence. Third, intermittency in free turbulent shear layers indicates the presence of a thin, sharp interface between turbulent fluid and irrotational fluid. This finding leads to questions about whether such sharp interfaces can be represented as a diffusive effect. Finally, the recent discovery that coherent structures dominate flows which were previously believed to approach pure turbulence directly causes us to reconsider the basic assumptions in the classical theory of turbulence.

The search for new concepts of the nature of turbulence has centered on understanding the mechanisms of the transition to turbulence in several simple fluid flows. Shear flows generated by splitter plates and round jets (e.g., Brown and Roshko, 1974; Browand and Weidman, 1976; Roshko, 1976; Fiedler and Wignanski, 1970) exhibit all of the troublesome intricacies associated with the transition and in addition are particularly appropriate for practical applications. Both larger and smaller scales of chaotic fluid motion develop in these systems. Flow near the orifice may initially be laminar for even high Reynolds numbers, and several distinct transitions are easily discerned before the onset of an apparently fully turbulent shear layer. It is still quite difficult, however, to pinpoint at which point in the flow the label "turbulent" is applicable. Indeed, coherent structures of large scale have been found to dominate well downstream in flows which appear

chaotic on smaller scales. By using similarity arguments, for example, we see that the splitter plate flow is always dominated by ever larger coherent structures. Through flow visualization experiments, a great deal of insight has been achieved into the exact mechanisms involved in the individual instabilities as well as some indication of the sequence of appearance of various scales of motion.

Although the flows near the orifice may be laminar for both jets and splitter plates, the shear layer generated is unstable to the Kelvin-Helmholtz instability. Small perturbations in the flow grow into nonlinear waves which break and roll up, transforming the original vorticity of the shear layer into isolated clumps. The primary wavelength generated by the instability is usually that of the fastest growing mode for that particular geometry or of some impressed wavelength determined by boundary conditions or initial conditions. Further development of the shear layer proceeds through the pairing of vortex clumps, a process which may be repeated many times downstream. One of the effects of pairing is to generate subharmonics of the original unstable wavelength, but smaller wavelength disturbances are created as well. These disparate wavelengths arise from at least two causes: imperfect pairing due to small fluctuations in the flow leaving an unpaired vortex which then merges with a previously formed pair (Browand and Winant, 1973), and the generation of small-scale disturbances in the interaction of the cores of the two vorticity clumps (Zabusky, 1981; Overman and Zabusky, 1981).

It should be emphasized that the flow may remain two-dimensional throughout this process, and that the rich frequency content of the flow has been produced by the action of only a few two-dimensional instabilities. As

a matter of practical importance, however, the flow almost always becomes three-dimensional when the Reynolds number is high enough. Three dimensional instabilities generally begin to play a role about the same time that visible vortex pairing ceases. This is primarily because the two-dimensional vortex rolls or loops are deformed by wave instabilities in the third dimension or by the presence of boundary conditions imposed by the system size. As these deformations grow, further two-dimensional pairing becomes difficult to observe and growth in the third dimension seems to be preferred. The non-linear growth phase for the three-dimensional instabilities is marked by increasing entanglement of vortex lines or loops, and the flow becomes more strongly turbulent.

The shear layer grows as vortex cores entrain irrotational fluid into the shear region. On the macroscopic scale the random walk of long vortex cores or filaments spreads the region containing the vorticity. This process resembles an eddy diffusion of vorticity at scales longer than the dominant scale of the eddies responsible for the transport. Representing this convective phenomenon as microscopic diffusion at short scales is incorrect, however, because random walk mixing increases these gradients rather than reducing them. The eddy diffusion-mixing length models work surprisingly well macroscopically because the diffusion is nonlinear, and the eddy coefficient is large where the macroscopically averaged vorticity is large. The front which propagates from such nonlinear diffusion can be sharp and hence has the potential to represent the thin transition between rotational and irrotational fluid. True vorticity diffusion enters into the picture only at the smaller scales, transporting vorticity into the continually thinning irrotational layers of fluid which have been engulfed.

In the work presented below, we describe numerical simulations of two-dimensional shear flows which go unstable through the Kelvin-Helmholtz instability. Our goal is to produce accurate enough calculations of the time-evolution of the major physical quantities so that we can analyze the flow behavior and test our concepts of the transition to turbulence. We consider two geometries: cylindrical, such as the round jet, and Cartesian, such as the splitter plate. In particular, we are interested in the initial transient behaviour and in the resulting unsteady pattern of structures.

III. THE NUMERICAL MODEL

The code FAST2D was used to perform the shear flow calculations described below. This code consists of a solutions of the time-dependent conservation equations for mass, momentum and energy coupled to algorithms describing gravity, molecular and thermal diffusion, and chemical reactions with energy release. These various parts of the code are coupled by timestep splitting and can be turned on or off independently by logical controls, as required by the problem to be studied.

The continuity equations are solved using the FCT algorithm JPBFACT, an advanced version of ETBFCT (Boris, 1976a). FCT is a finite-difference technique for solving the convective equations which is particularly useful in problems where sharp discontinuities arise and are maintained throughout the calculations. These discontinuities may be shocks or contact surfaces. In the case studied here, we are concerned with interfaces in material density. The algorithm modifies the linear properties of a high order algorithm by adding sufficient diffusion during convective transport to prevent dispersive ripples from arising, and ensures that all conserved quantities remain monotonic and positive. This added diffusion is subtracted out appropriately where not needed in an antidiffusion phase of the timestep to maintain second order accuracy.

Another important feature of the FCT algorithms is their ability to divorce the grid motion from the fluid flow. This freedom has been used to incorporate variably spaced grids as well as adaptive grids (Book et al., 1980; Oran et al., 1982) which automatically follows regions where there are sharp gradients and more resolution is needed. In transition to turbulence calculations, this means that realistic spatial inflow and outflow problems

can be solved rather than the more idealized periodic problems where temporal but not spatial problems can be considered.

The JPBFACT routine solves the one-dimensional continuity equation in Cartesian, cylindrical, spherical or generalized nozzle geometries, depending on the value of a logical switch. Since the algorithm is one-dimensional, timestep splitting in the various directions is used to construct two- and three-dimensional codes. The two-dimensional Cartesian and cylindrical calculations are actually performed with the same code, but with the particular type of geometry specified at the beginning of the calculation.

In the calculations presented below, the grid spacing was set up at the beginning of each calculation and held fixed in time. In general, the cell spacing should not change more than 20-30% from cell to cell. For the Cartesian calculations used to model the splitter plate experiments, finely spaced cells were clustered around the centerline where the instability first occurs and the coherent structures form. For the cylindrical calculations used to model the gas jet, the grid was finely spaced in the jet and through the region of the shear. Sample grids are shown in Figures 1 and 2.

In the calculations presented below, the gravity, diffusion, chemistry, and energy release options included in the code are not used. Thus we will not describe them in great detail in this report. However, we note that the algorithms for chemistry, energy release and diffusion have been discussed by Cran and Boris (1981).

IV. OUTFLOW BOUNDARY CONDITIONS

Solving fluid dynamics problems with realistic outflow boundary conditions has always been difficult. The fundamental problem is that information about the flow beyond the computational mesh is required to make the fluid near the boundaries behave properly. There are a number of ways to handle this problem, and they generally, like FCT, involve using guard cells which are not actually part of the calculation but which tell the boundary cells of the computational mesh how the outside world is behaving. The simplest model of outflow in guard cells is to say that the momentum, energy, and density do not change, i.e., there is effectively zero gradient. This can cause problems in long time calculations since it does not provide for the fact that as we go further from the phenomena being computed, the system relaxes to background conditions.

Here we present an outflow algorithm developed to use with the FCT algorithm described in the last section. The outflow algorithm incorporates the requirement that the solutions must relax toward ambient conditions. Then the strong nonlinear stabilizing properties of the FCT method appear to eliminate instabilities which occur in other nonlocal methods when low order extrapolations are used for specifying boundary conditions (Tukel, 1980). The types of fluid problems for which the outflow algorithm is intended can be written as a coupled series of single or multi-dimensional continuity equations of the form

$$\frac{dQ}{dt} = - \nabla \cdot (Q\underline{v}) + \text{Source} - \text{Sinks} \quad (1)$$

where the compressible fluid must somewhere flow off the edge of the computational region. In this equation Q is a conserved quantity such as the mass, momentum, or energy and v is the vector fluid velocity. The major requirement of the algorithm is that the fluid must be represented in the region off the grid by fictitious "guard" or "ghost" cells. These values are used to compute the derivatives and gradients in the computational cells which are on the edge of the grid. Throughout the discussion, we let the last cell on the grid be cell N . The subscript g will be used to indicate the guard cell.

The linear extrapolation for outflow,

$$Q_g = Q_N + (Q_N - Q_{N-1}) \quad (2)$$

is unstable when used in conjunction with most numerical methods for advancing the grid variables. Even the zeroth-order extrapolation,

$$Q_g = Q_N \quad (3)$$

is unstable in the sense that the algorithm has no knowledge of the physically correct asymptotic value of Q , and hence the flow cannot ever be expected to relax to ambient conditions.

The formula tested here is a simple zeroth-order extrapolation plus a slow local relaxation toward the known ambient value Q_{amb} .

$$Q_g = Q_N + \frac{v_{char}}{L_{char}} \cdot \Delta t \cdot (Q_{amb} - Q_N) \quad (4)$$

Here L_{char} is a characteristic scale for the flow causing the relaxation to ambient, and v_{char} is the velocity of this relaxation. The quantity v_{char} is typically the local sound speed for the pressure or flow velocity for an entropy or species variable. This expression is an approximation to the

lowest order terms in an asymptotic expansion. It is valid for times long compared to a sonic transit time of the system.

Two types of test calculations are presented: 1) a diaphragm breaking in a barrel which releases a high pressure, supersonic gas into a low pressure background, and 2) a cylindrical jet in which a lower density gas flows into a quiescent background. The validity of the algorithm is shown by comparing nested series of calculations where the outflow boundary of one grid is interior to the flowfield of a larger grid. The first problem, the diaphragm in a barrel, is not a shear flow problem. However, it is included in this paper because it is an initial test of the outflow algorithms used.

V. TEST OF THE OUTFLOW ALGORITHM: DIAPHRAGM IN A BARREL

1. The Test Problem

Below we compare a nested series of calculations where the outflow boundary of one grid is interior to the flow field of a larger grid. Then the approximate solution, obtained using the outflow boundary condition, can be calibrated against the "correct" solution obtained before spurious information from the outer computational boundary arrives at the outer edge of the smaller grid. Calculations with three different size grids are presented, a 40 x 40 grid, an 80 x 80 grid, and an even larger 150 x 300 grid.

A set of four runs using the FAST2D model have been performed. The problem chosen is cylindrically symmetric and simulates the fluid flows which occur when a thin diaphragm bursts. The diaphragm initially confines a high pressure, isothermal gas in a thick-walled barrel. The general properties of the four different types of computations performed are given in Table I.

Table I.

<u>Calculation</u>	<u>Grid Size</u>	<u>Boundary Conditions</u>	<u>Comments</u>
#1	40 x 40	Reflecting walls	
#2	40 x 40	Outflow Algorithm	Test of new outflow algorithm
#3	80 x 80	Outflow Algorithm	Calibration for Run #2
#4	150 x300	Reflecting walls	Calibration for Run #3

The results discussed in this section are illustrated by digitized contour plots of the density. Consider Figure 3, which is a schematic diagram of the initial conditions for the test problem considered in this section. In this and the figures following, different typed letters in the computational cells combine to form a 'shadowplot' where the boundaries between two different characters represent contours of the fluid density. Table II lists the letters used and the density ranges they span in all the figures in this Section. The letter "I" is used for alternate bands to improve the resolution.

Table II.

Shadowplot Contour Levels:*

1.00E-03 <	< 1.45E-03	1.45E-03 <	- < 2.10E-03
2.10E-03 <	+ < 3.20E-03	3.20E-03 <	* < 4.80E-03
4.80E-03 <	A < 7.00E-03	7.00E-03 <	I < 1.00E-02
1.00E-02 <	B < 1.45E-02	1.45E-02 <	I < 2.10E-02
2.10E-02 <	C < 3.20E-02	3.20E-02 <	I < 4.80E-02
4.80E-02 <	D < 7.00E-02	7.00E-02 <	I < 1.00E-01
1.00E-01 <	E < 1.45E-01	1.45E-01 <	I < 2.10E-01
2.10E-01 <	F < 3.20E-01	3.20E-01 <	I < 4.80E-01
4.80E-01 <	G < 7.00E-01	7.00E-01 <	I < 1.00E+00
1.00E+00 <	H < 1.45E+00	1.45E+00 <	I < 2.10E+00

*E.q, read "E-03" as 10^{-3}

The initial conditions are the same for calculations #1-4. The ambient density is $1.29 \times 10^{-3} \text{ g/cm}^{-3}$, the pressure is a fixed multiple, 1.0×10^9 , of the density, and the lower half of the barrel is pressurized to 1000 times the ambient pressure. The barrel geometry is the same for all cases listed in Table I. The spacing of the computational grid, 0.1 cm, is also fixed in all the computations. The cases listed in Table I differ only in the location of the upper and right hand boundary and in the boundary condition applied.

2. The Outflow Algorithm

The conserved quantities were convected by FCT in this problem: the mass density, ρ , and the two components of the momentum density, ρv_x and ρv_y . The characteristic velocity for relaxation of density and pressure fluctuations is the sound speed, here constant at $3.2 \times 10^4 \text{ cm/s}$. The characteristic length was taken as the radius of the cylinder, 4.0, 8.0, and 15.0 cm for the three different sized grids. The density was extrapolated beyond the end of each exterior row or column by

$$\rho_g = \rho_N + \frac{C_s}{R_{\text{wall}}} \cdot \Delta t \cdot (\rho_{\text{amb}} - \rho_N) \quad (5)$$

$$(\rho v_r)_g = (\rho v_r)_N \quad (6)$$

$$(\rho v_z)_g = (\rho v)_N \quad (7)$$

where C_s is the sound speed. Since the pressure and density are proportional to each other, the pressure is extrapolated as in Eq. (5).

3. Results of the Calculations

Figure 4 shows a series of shadowplots from Calculation #1, which has reflecting walls. Figure 4A shows that after 25 timesteps the shock has moved only about 5 cells up the barrel (0.5 cm) and has not yet reached the rim. By step 50, shown in Figure 4B, the flow inside the barrel is still essentially one-dimensional. However, as the shock and following supersonic flow emerge from the barrel, the first evidence of the multidimensional nature of the flow is evident. By step 100, shown in Figure 4C, the flow has hit the upper boundary and the rarefaction is working its way back toward the bottom of the barrel. By step 200, shown in Figure 4D, the primary shock has had time to rattle back and forth between the solid barrel wall and the outer and top boundaries, which here are solid walls.

Figure 5 presents a series of shadowplots taken from Calculation #4, performed on the 150×300 grid. These plots show the solution of the outflow test problem without any interference from the boundaries. The barrel wall and the nested 40×40 and 80×80 computational regions are outlined on this figure. Note that of the 150×300 cells used in the computation, only 128×215 are shown on the figures.

Figures 6 through 10 are composites of the different calculations at fixed timesteps. Calculations #2 and 3 have the outflow boundary conditions at the upper and right hand walls. From Figure 6 we see that by step 100 the shock would have reflected from the top wall in Calculation #1. Comparing Figures 4 and 6, we see that by this time the reflection from the closed wall in Figure 4 has affected the answers down to about cell 34 on the Z axis. Within and just outside of the barrel, the solutions are still essentially the same. Calculation #3 in Figure 6 shows that the expanding plume has

reached cell 65 ($Z = 6.5$ cm) and so the flow is still interior to the 80×80 grid. At this point no errors have propagated back from this boundary into the interior region. The outline of the region considered in Calculations #1 and #2 are shown in this figure. Calculation #3, which uses the 80×80 grid, and the new outflow boundary conditions, provides a calibration of the open boundary condition used in Calculation #2. Thus we can here compare Calculations #2 and #3 in Figure 6 and see that they show substantially the same result.

In Figure 7 (step 150), Calculation #3, the rarefaction behind the primary shock is well formed and appears as a white strip starting from the outer corner of the barrel wall. Reflection off the upper boundary at $Z = 8.0$ cm would have occurred by this time if the upper wall had been a reflecting boundary. In this case, where we are using a model for the outflow, we can see that small errors are beginning to move inward.

By step 200 in Figure 8, Calculation #3, the flow has exited through the upper surface but has not yet reached the outer wall. Some errors have been propagating toward the region of the 40×40 calculation on the larger 80×80 grid, but have not reached it yet. Thus this Figure is good for comparison with Figure 8, Calculation #2. The extent of the outflow boundary condition errors at the boundary of the 80×80 region is found by comparing with Figure 8, Calculation #4.

By step 300 in Figure 9, Calculation #2, the primary shock has spread down around the barrel and has reached the ground plane at $Z = 0.0$ cm. The errors which are generated by the open boundary conditions should have reached the 40×40 region by now, yet Calculations #2, 3, and 4 are still essentially identical.

Finally, by step 400 in Figure 10, Calculation #3, the errors from the outflow boundary conditions have reached the vicinity of the barrel. Comparison with Figures 10, Calculations #2 and 4, show only small differences which can be associated with the outflow boundary algorithm we are testing. The accuracy of this result in the 40×40 case is surprising where the computational boundary was closer than a barrel diameter at every point.

VI. TEST OF THE OUTFLOW ALGORITHM: CYLINDRICAL GAS JET

1. The Test Problem

The test problem described above is related to interior ballistics, atmospheric explosions and airblast problems as well as shear flows. It shows our first application of these boundary conditions in an important problem where both supersonic and subsonic flows are important. The flows were dominated by divergence rather than rotation, and the relaxation was primarily by acoustic waves rather than convection of vortices off the system boundary. The excellent results obtained from these tests encouraged us to proceed with the difficult subsonic problems described here in this Section. In combustion problems, expansion and vorticity are equally important. Thus we felt that the separate tests of both fluid dynamic aspects was appropriate.

The Kelvin-Helmholtz outflow tests presented in this section were done in preparation for transition to turbulence calculations such as those presented in the next section. We wish to test the boundary condition algorithm described above in a calculation in which the flows are subsonic throughout the course of the calculation and hence the flow is essentially incompressible. Here we consider a jet of neon gas moving at 2×10^4 cm/s which is vented into a quiescent air background. There is a small initial perturbation at the interface between the jet and the air which causes the the shear flow eventually to become unstable. After a longer time, the usual pattern of rotating coherent structures forms at the interface. These structures merge and flow out of the computational system, i.e., off the top of the computational mesh.

2. The Outflow Algorithm

The basic outflow algorithm used in this case states that the pressure in the guard cell just across the boundary is extrapolated from the boundary cell but relaxes to a prespecified ambient value. Specifically,

$$P_g = P_N + \omega \cdot \Delta t \cdot (P_{amb} - P_N) \quad (8)$$

and

$$\omega = \frac{C_s}{R'} \quad (9)$$

where P_g is the guard cell pressure, P_{amb} is the ambient pressure, and P_N is the boundary pressure. Here ω reflects the rate of relaxation and is controlled by the sound speed, C_s , and a characteristic radius, R' . We have taken R' as the characteristic radius of the disturbance, in this case the radius of the nozzle. Since the flows here are typically a third to a fourth of the speed of sound, the outflow velocity for vorticity can be estimated using the sound speed. For slower flows the fluid velocity should be used. The guard cell pressure, Equation (8), then effects the calculation of the guard cell energy value. The relaxation rate ω is an adjustable parameter representing the characteristic rate and size of flow patterns leaving the grid and presumably could be adjusted to improve the match between large- and small-grid calculations still further. The density and momenta are extrapolated according to

$$\rho_g = \rho_N \quad (10)$$

$$(\rho v_x)_g = (\rho v_x)_N \quad (11)$$

$$(\rho v_y)_g + (\rho v_y)_N \quad (12)$$

Note that in this case unlike the barrel calculation previously described, pressure and density are decoupled. Thus to account for effects of sound waves, we need to modify only the pressure at the boundary. Modifying the density has little or no effect because there is no substantial inflow of mass except at the nozzle.

3. Results of the Calculations

In order to test the outflow boundary conditions algorithm, we performed a series of three calculations summarized in Table III. In the first and largest calculation, a stretched 60×120 mesh represents a region 7.6 cm in radius by 26.0 cm in length. The second calculation was initialized by using the results from step 2000 of the first calculation, but uses only the first 54×100 cells of the original mesh. Thus it represents a volume of 3.25 cm radius by 10.8 cm length. The final calculation used a 54×100 mesh, equivalent to the mesh used in Calculation #2. However, this last calculation was started from step = 0 with the smaller mesh.

Table III

Calculation	Grid Size	Comments
#1	60×120	Step 0 - 3000
#2	54×100	Steps 2000 - 3000 Restarted from step 2000 of #1
#3	54×100	Steps 0 - 3000

In order to compare the results of the two calculations, we present contours of the quantity

$$R = \frac{n(1)}{n(1) + n(2)} \quad (13)$$

where $n(1)$ is the number density of neon and $n(2)$ is the number density of air, where air was taken as one species with the mean properties of a mixture of 20% O₂ and 80% N₂. By definition, the contours range from $R = 0$, 100% air, to $R = 1$, 100% neon. Figure 11 shows the ratio R for Calculation #1 at steps 500, 1000, 2000, and 3000 and presents a time history of the flow. We see that the system initially goes unstable at 1.14 cm from the nozzle. The structures grow, merge and finally exit out of the top of the computational grid. We have set the inflow velocity to 2×10^4 cm/s. It takes ~ 1000 time steps for a fluid element entering the system at the nozzle to reach the top of the large grid, 26 cm if it is not slowed appreciably in interaction with the background air. Thus much of the material entering at step 2000 will be exiting the computational grid shortly after step 3000. The material effectively changes over every 1000 steps. Thus the calculation was continued far enough to test the boundary condition algorithm for long term fidelity and stability.

Figure 12 shows a comparison of step 3000 for calculations #1, 2, and 3. First we note that the first two figures look very similar within the 54×100 range, which is very encouraging. The last figure, on the far right, however, while qualitatively similar to the first two, has differences. Figure 13 shows a composite for the 54×100 and 60×120 calculations, starting at step 500 through step 1500. Through steps 1000 the calculations are quite similar, however small but noticeable differences begin to appear between steps 1000 and 1500.

4. Discussion

The constants chosen in implementing the boundary conditions may not have been the best ones and this has to be tested. First, the value of R' should probably be larger than the radius of the inlet. This value should reflect the characteristic sizes of the structures, and we know that they grow according to a similarity condition. Also, the appropriate velocity to use would be the fluid velocity, not the speed of sound, if the vortices were leaving the region at very slow speed. The speed of sound was appropriate in the barrel problem because that was a problem in supersonic flow. Here we are concerned with subsonic flows.

The shear flow discussed in this section is unstable and will always go unstable as long as there is some small perturbation, even just noise or roundoff, between the flowing and quiescent gas. However, unlike the diaphragm in the barrel problem discussed above, the exact appearance of the Kelvin-Helmholtz instability in the nonlinear regime is very sensitive to background conditions, initial conditions, and to small fluctuations in the system. This is the crux of the problem in experiments also: many realizations are possible depending on fluctuations in the initial and boundary conditions. In these situations some of the difficulty encountered in doing the computations reflects the same difficulty in the experiments. Both highlight the highly nonlinear sensitivity of the system to the boundary conditions.

VII. GAS JET AND SPLITTER PLATE SIMULATIONS

In this section we describe preliminary results obtained using the model described above to simulate the coherent structures developed from Kelvin-Helmholtz instabilities in shear flows. In the previous section, we emphasized numerical methods; here we emphasize the physical results. We discuss two configurations of the FAST2D model discussed above: a cylindrical gas jet and the Cartesian splitter plate geometry.

1. Splitter Plate

Figure 14 shows a sequence of frames from a two-dimensional simulation of the flow generated at an idealized splitter plate. The tip of the splitter plate is located at $x = 0.0$ cm and $y = 4.0$ cm, the dividing point between the light gray fluid entering into the lower half of the computational region (air at high velocity) and the darker gray fluid (air at somewhat lower velocity). Figure 2 shows the type of variably spaced grid used near the trailing edge to represent the Cartesian splitter plate problem. The y-direction has good resolution near the centerline. The velocity of the lower stream is 1.5×10^4 cm/s and the upper stream is considerably slower, flowing from left to right at 5×10^3 cm/s. As the large spanwise vortices propagate downstream, they merge and grow. Therefore the larger computational cells encountered by the flow further downstream and further from the centerline will be adequate to resolve the larger coherent structures about as well as the smaller structures are resolved near the splitter plate.

The initial stages of the development of the flow are not shown in Figure 14. During this early period, before 0.87 ms, the shear flow established by the trailing edge of the splitter plate is initially restricted to a very narrow layer which broadens quickly at first due to viscosity and then

more slowly as both streams of fluid leave the splitter plate. As in the case of the cylindrically symmetric jet simulations discussed in the boundary condition test problem and in the next section below, the flow is Kelvin-Helmholtz unstable. Initially, during the linear growth period of the instability, most of the computed region behaves as if there were periodic boundary conditions because the impressed perturbation has a wavelength short compared to the system length. By 0.87 ms, the first panel in Figure 14, the influence of the inflow and outflow is felt. Merging vortices move off the right edge of the computational system and unperturbed fluid moves in on the left.

Our preliminary calculations used boundary conditions which prespecified values for the mass, momentum and energy density of the inflowing gas. These conditions, however, did not correctly provide the feedback from the Kelvin-Helmholtz rolls and vortex merging on to the newly entering fluid. We know that pressure pulses from upstream create small transverse flows at the trailing edge of the splitter plate. These pulses, then, start the instability at finite amplitude for the next coherent vortex roll up. When the inflow pressure was specified as ambient, we observed that the first vortex structures formed very far downstream. The apparent reason for this was that the pressure perturbations arriving at the inflow boundary were cancelled by the non-physical condition of specifying the inflow pressure. Clearly a more physically reasonable treatment of the inflow response to pressure fluctuations as well as the outflow was required for this type of problem.

The more correct way to treat the inflow is to specify the inflow density and velocity, and then to use a zero slope condition on the pressure at the inflow boundary to derive the energy. This algorithm was used for all

the simulations which follow. It allows pressure differences between the top and bottom streams to generate transverse flows and implies that the physical plenum admitting the gas into the region we are simulating is of zero length. Physical treatment of a real plenum could be added by extending the splitter plate into the computational region. A simple lumped parameter boundary calculation representing the real plenum could also be developed using the more detailed model to calibrate it. Then a phenomenology would be incorporated to estimate the pressure build up and velocity changes which could be expected on inflow. Thus we see that the pressure reflection condition is one limit of such a model for which the plenum has zero volume. This limit is appropriate when the fluid flow is slow compared to the sound speed, the situation most often considered in experiments but not necessarily applicable when the flows are as fast as in this calculation.

The outflow boundary conditions were handled as described in the previous sections of this paper. With a fluctuating inflow pressure it is important to relax the outflow pressure toward an ambient value. This is because a background, base pressure for the system has to be specified in compressible calculations when the inflow pressure is allowed to float in response to pressure waves from upstream. Relaxation of the density and momentum toward ambient is less important on outflow because these values are given at the inflow boundary. The long time values of all the variables must be available to the solution from the beginning to prevent secular deviation of the calculated flow from properties characterizing the ambient medium.

The mechanism which reinitiates the instabilities close to the inflow boundary works through pressure pulses generated at various scales by the fluid accelerations involved in nonlinear vortex rollup and vortex merging

downstream. They are required to ensure that the flow remains essentially divergence free everywhere when a coherent structure or vortex is locally accelerated. Though these pulses are transmitted acoustically, they exist even in the incompressible limit.

Evidence for this mechanism is supplied by the sequence of density shadowplots shown in Figure 14. By 0.87 ms the initial linear growth phase is over and the instability has saturated rather uniformly along the original slip line. States similar to what occurred in this calculation prior to 0.87 ms are shown in the following section on the evolution of the instability in the round jet. In the splitter plate calculation, a long unrippled portion of the interface is seen on the left of the 0.87 ms panel, showing that the initial instability has flowed away from the trailing edge. However, the pressure perturbations resulting from this were small and short scale, so that they did not initiate the Kelvin-Helmholtz instability strongly enough for small scale vortices to appear on the left of the 0.87 ms panel.

The first vortex merging is also shown approaching the right hand boundary in the top three panels of the figure. This flow structure is both large and irregular enough to generate stronger pressure perturbations, which can be seen driving noticeable fluctuations into the left half of the interface at 0.98 and 1.03 ms. By the last frame at 2.06 ms, a spectrum of modes is seen in what looks like a snapshot from an experimental flow visualization.

2. Gas Jet

First we consider the coherent structures in the transition from laminar to turbulent flow in coflowing gas jets in two cases: air into air, which is constant density, and air into freon, where the density ratio is about 6:1.

These simulations were performed in order to isolate and study the effects of density gradients, which is one of the the major physical conditions distinguishing reactive flow from classical turbulence. The calculations also provided important information on the application of inflow and outflow boundary conditions to subsonic shear flow problems.

In the first case, air into air, the densities are constant and these density gradients do not exist. However, the second case, air into freon, a light gas into a heavy gas, has the added effect of vorticity generation through the term

$$\frac{d\xi}{dt} = \frac{\nabla\rho \times \nabla P}{\rho^2} \quad (14)$$

where ξ is the vorticity, and ρ and P are the fluid density and pressure fields, respectively.

The geometry is the same as in the gas jet described in Section VI. The air flows into the cylinder from a hole at the bottom center at a velocity of 1.5×10^4 cm/s. Unlike the problem discussed in Section VI, in which the jet flowed into a quiescent background, the fast jet of air is surrounded by a co-flowing jet at the much lower velocity of 5×10^3 cm/s. The co-flow is either air or freon. Also, the right hand boundary here is a hard wall with only the top boundary open.

The instability in the fluid is generated by imposing a small sinusoidal perturbation on the momentum at the interface, initially at $r = 0.6$ cm. This divergence free perturbation is largest at the material discontinuity and goes smoothly to zero at the sidewalls and at the center of the system. The

maximum amplitude of the perturbation is 2% of the jet velocity. Given the initial density and the momentum perturbation, an incompressible velocity perturbation is implied.

Figures 15 and 16 summarize the air into air and the air into freon calculations we wish to discuss. The first effect observed in these calculations is the formation of a Kelvin-Helmholtz instability at the slip line. Because of the short wavelength and fixed amplitude of the perturbation, the problem initially evolves as a periodic, time dependent system except for one or two instability wavelengths at each end. The first panel of Figure 15 (the air into air cylindrical jet) shows this effect at 240 μ s. Here a rather uniform band of mixed material forms separating the two fluids. This uniform buffer zone does not initially display the vortex merging which characterizes the fully developed nonlinear flow. Indeed, a fully developed turbulent-looking flow is not set up until most of the jet material initially on the computational mesh has flowed out the top and been replaced by fresh material through inflow.

The two calculations look qualitatively different. There is a noticeable decrease in the entrainment in the air-into-freon calculation. The vorticity generated at the nozzle moves away at a density-weighted velocity intermediate between the velocity of the two streams. In the air into freon case, Figure 16, the sloped lines on the figure which track structures moving on interface show that these structures move more slowly than in the air into air case in Figure 15. As the coherent structures move with a density weighted velocity, the air into freon case has a much greater slip velocity between the jet and the coflow. As a result, for the air into freon case, the freon entrainment is reduced and the nonlinear coherent structures form

much closer to the nozzle lip. As can be seen from the sloped lines on the two figures, the velocity of the vortices is faster in the air into air case by about a factor of two. Because the air is moving much faster than the vortices in the air into freon case, relatively little freon gets entrained.

The calculation shown in Figure 16 shows a choking effect in which the dense coherent structures squeeze light material in the jet and push the jet flow outward at the nozzle. This again affects the lower boundary through the pressure reflection condition, and thus effects the inflow of material. Then the Bernoulli effect accelerates the jet fluid through the slowly changing channel formed by the slower, higher density coherent structures. The panel at 390 μ s on the lower left shows the jet accelerating so much that the density has dropped noticeably. A higher pressure region forms just above the nozzle to accelerate the jet axially through the constriction formed by the coherent structure. This higher pressure also pushed the interface laterally at the nozzle lip, as can be seen in the remaining panels of Figure 16. This displacement becomes the seed for the next coherent structure.

VIII. DISCUSSION AND SUMMARY

This paper has presented a summary of work to date at NRL on developing and testing a model to use for studies of unstable shear flows transitioning to turbulence. The main features of the model are that it is two-dimensional, fully compressible, and time dependent in either Cartesian or cylindrical geometry. To date, emphasis has been on development of the model as opposed to application, although some results and model predictions have been discussed in Section VII.

Future emphasis will be on applications although there is still much to be learned about inflow perturbations. In particular, we are interested in how well this model compares to experiments. Calculations using this model will be compared to experiments to test the effects of density differences on the initial instability and on transition to turbulence. We now know that it be necessary to add a number of other physical processes to the purely convective calculations shown above. For example, we might have to consider buoyancy and molecular diffusion. Buoyancy should be important at distances 8 to 10 nozzle diameters downstream, and molecular diffusion could be important when very light gas flows into a heavier gas. Algorithms for gravity, and molecular diffusion are currently a part of the model. We are currently developing subgrid turbulence models, and the particular inflow nozzle model will have to be developed in coordination with the experiments. Finally, computational diagnostics must be included that operate on the computed primitive quantities (such as mass, momentum and energy) and put them in a form that can be directly compared with the experiments. These diagnostics includes such quantities such as fluctuation velocities, correlations, and various averages.

We will also look at the effects of energy release, which occurs in reacting shear flows in combustors. Calculations with a model for heat release should at least qualitatively reproduce some of the bulk effects seen in the experiments (Yule and Chigier, 1979; Yule, 1981). For example, there is a noticeable extension of the turbulent transition region when there is chemical energy release.

In conclusion, we feel that we now have a tool which has been developed carefully and tested in a number of calculations. The limitations and remaining difficulties are reasonably well known.

ACKNOWLEDGMENTS

We would like to thank T.R. Young, J. Tittsworth, and H. Brock for their help in implementing FAST2D and with the graphics that made these results presentable. We would also like to thank Professors N. Chigier, P. Libby, S.S. Penner, J. Lumley and F. Gouldin for encouraging this project, and Drs. A. Wood, R. Miller, K. Ellingsworth, T. Coffey and R. Lau for supporting of this work. We thank J.M. Picone and J.H. Gardner for their careful preliminary reading of this manuscript. The calculations of round jets and splitter plates were performed under ONR project #RR024-03-01 and NRL project #RR011-09-43. Those calculations presented in Section V to benchmark the outflow boundary condition on the barrel problem were performed on the Reactive Flow Modelling Facility developed under joint ONR/NRL sponsorship, project #RR014-03-0F.

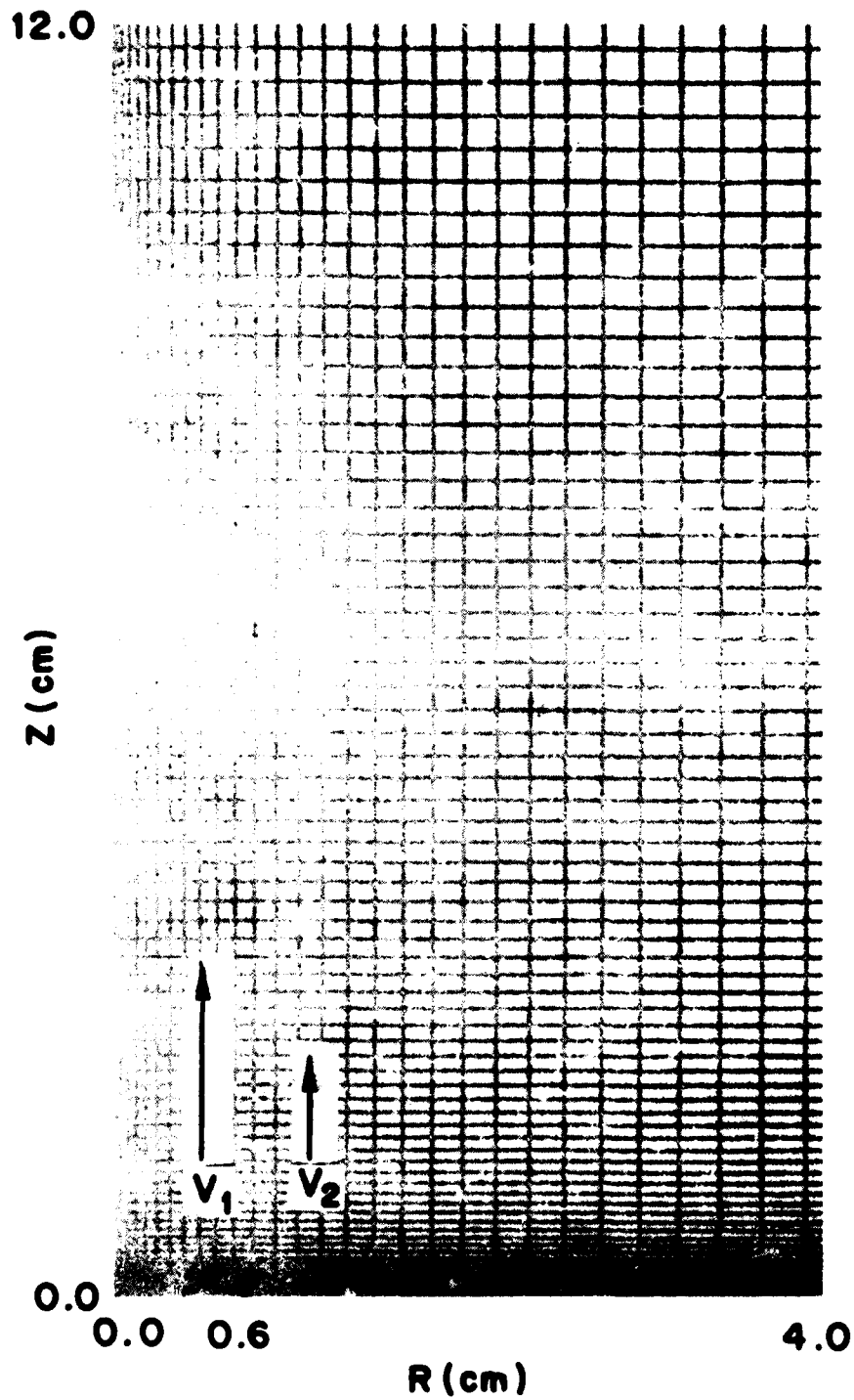


Figure 1. Sample computational grid used in the cylindrical calculations of the round jet.

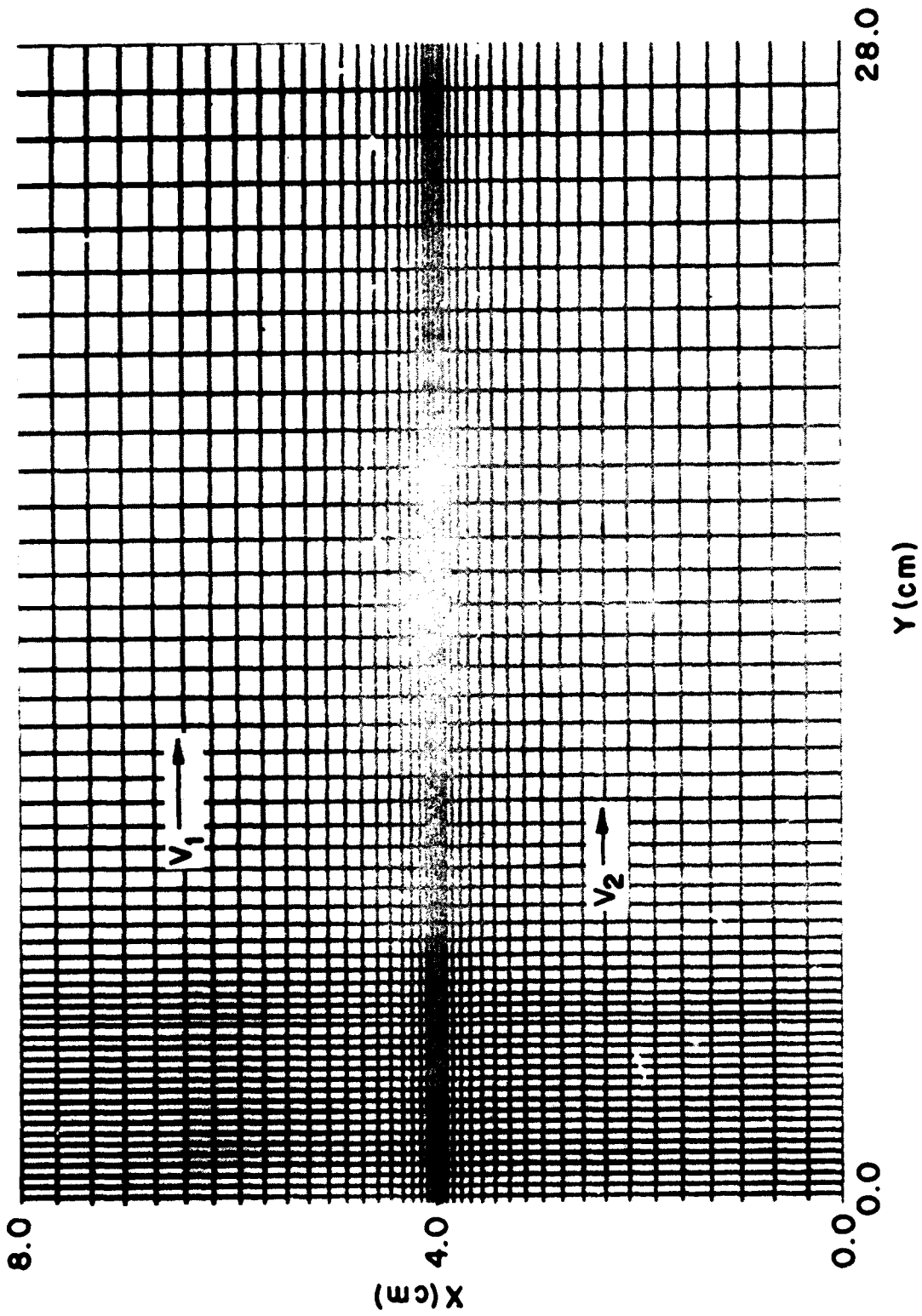


Figure 2. Sample computational grid used in the Cartesian calculations of the splitter plate.

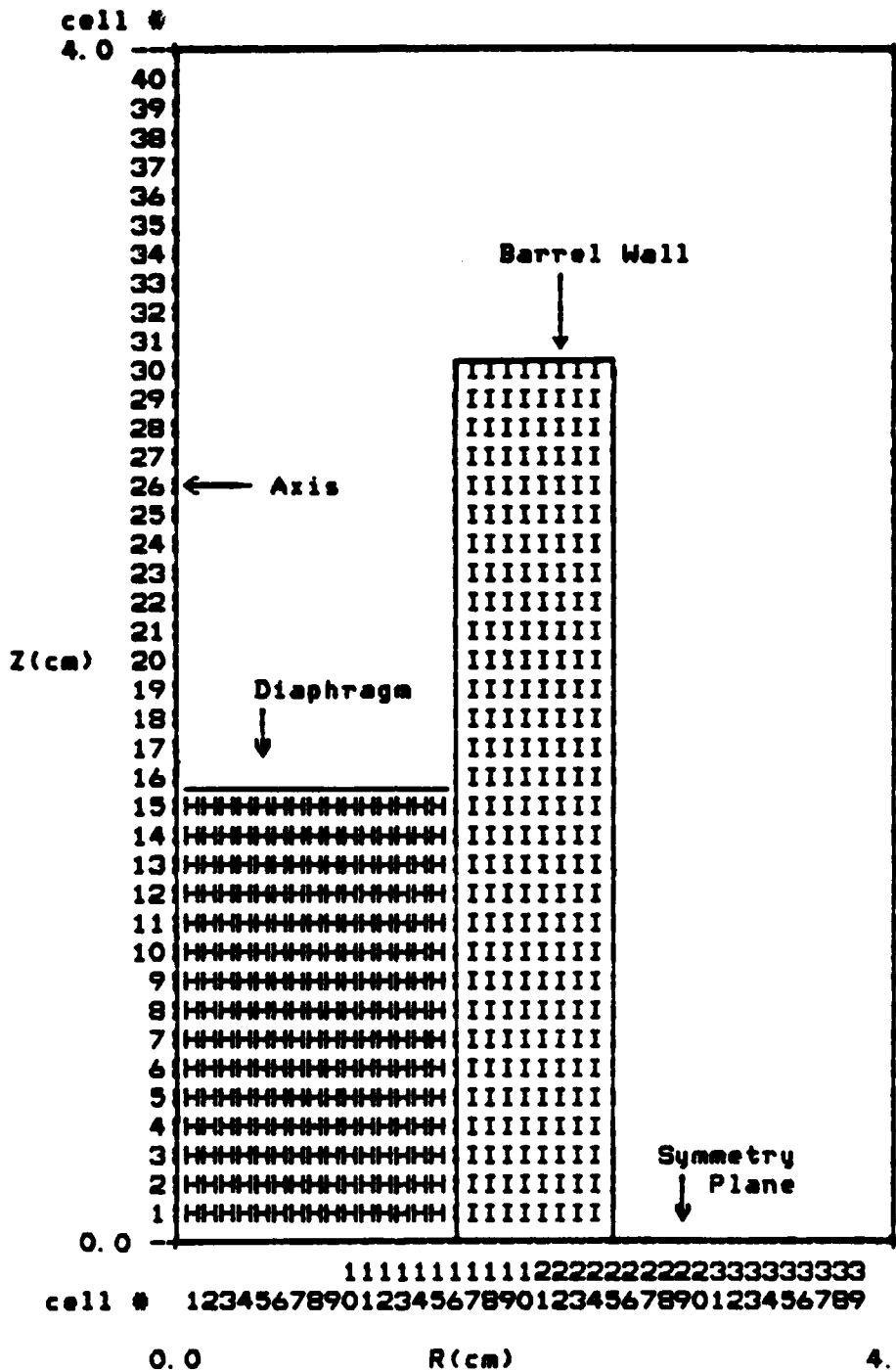


Figure 3. Initial conditions for the calculations of an explosion in a barrel. The outer and upper walls are solid in Calculations #1 and #4. Calculations #2 and 3 use the outflow algorithm at the upper and outer walls.

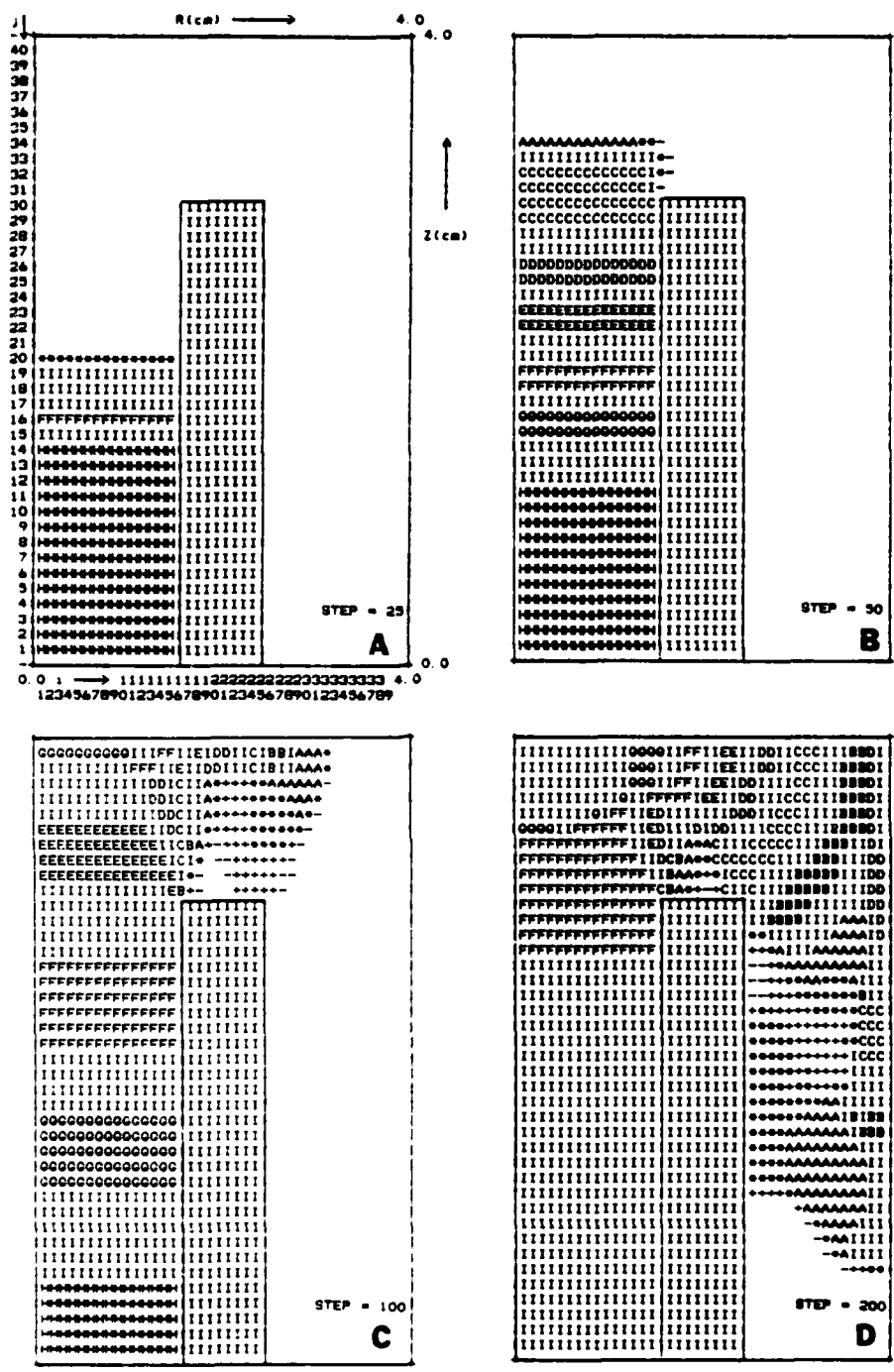


Figure 4. Barrel explosion problem for Calculation #1 at four times in the calculation. Reflection from the top and right hand side is observed in C and D due to the solid walls.

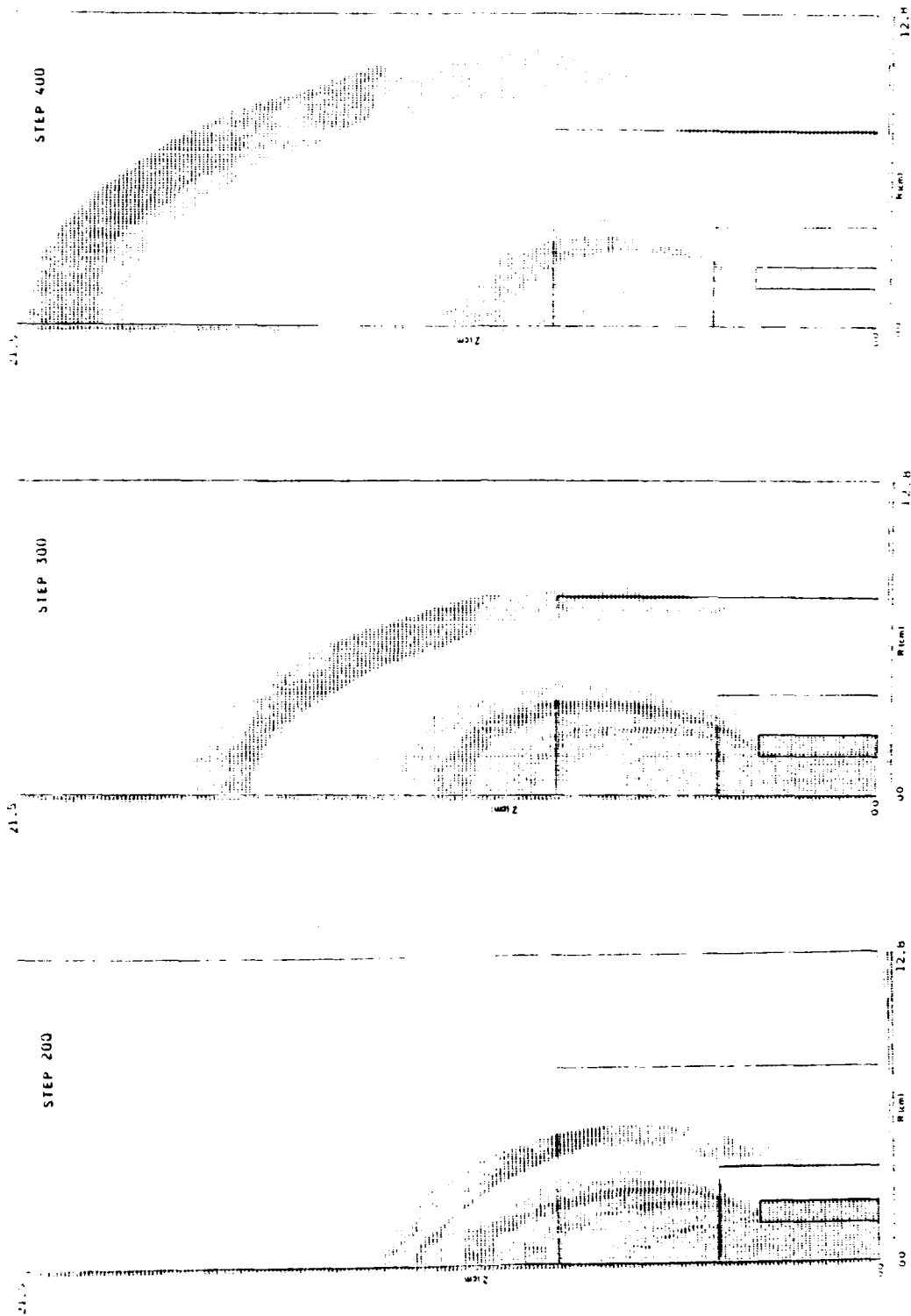


Figure 5. The same barrel calculations on the very large 150×300 grid for three times in the calculation. Notice that only 128 x 215 cells are shown. Through step 400 the shock does not leave has not hit the calculation boundaries.

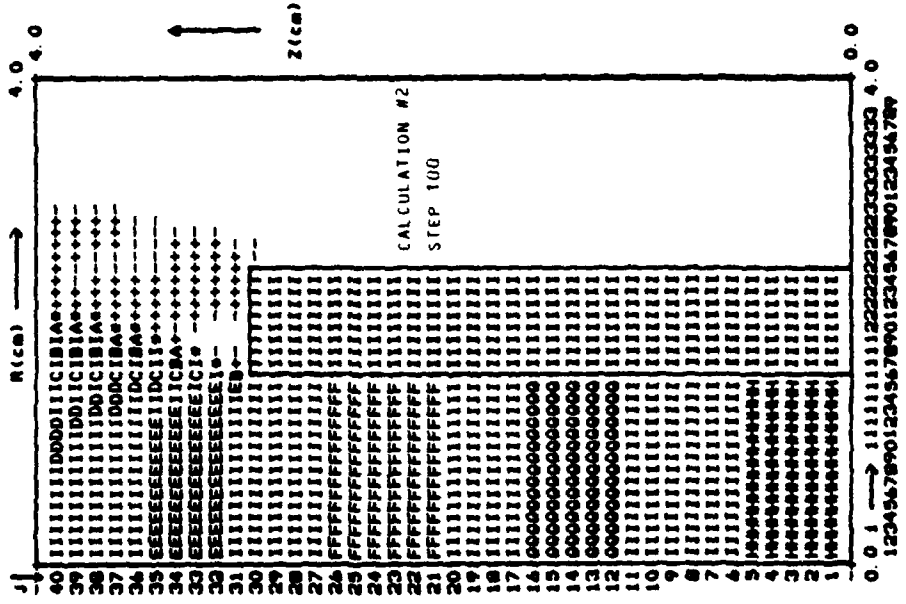
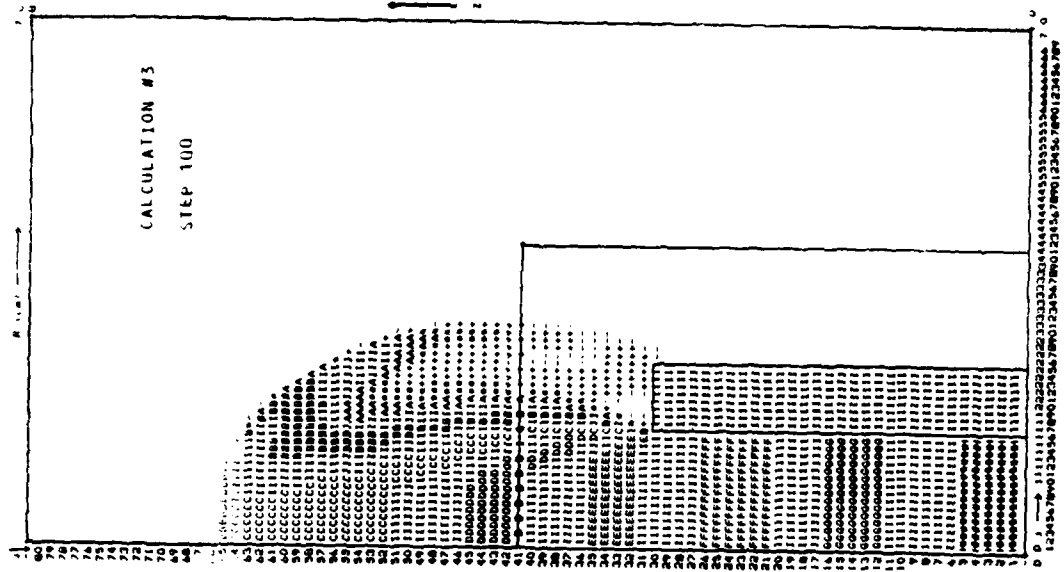


Figure 6. Step 100 for barrel Calculations #2 and 3.

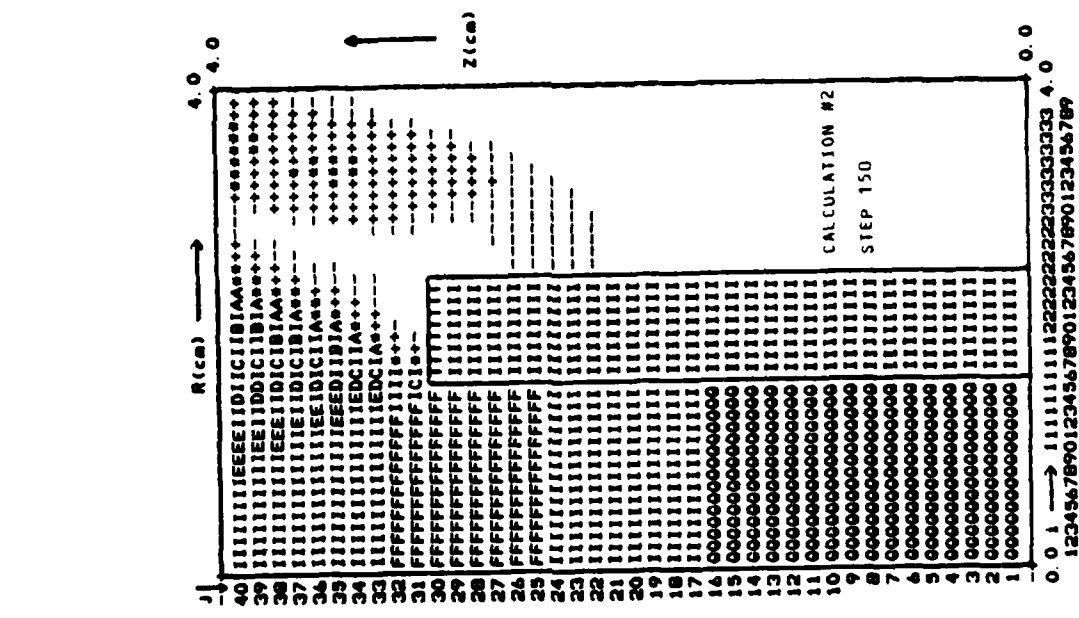
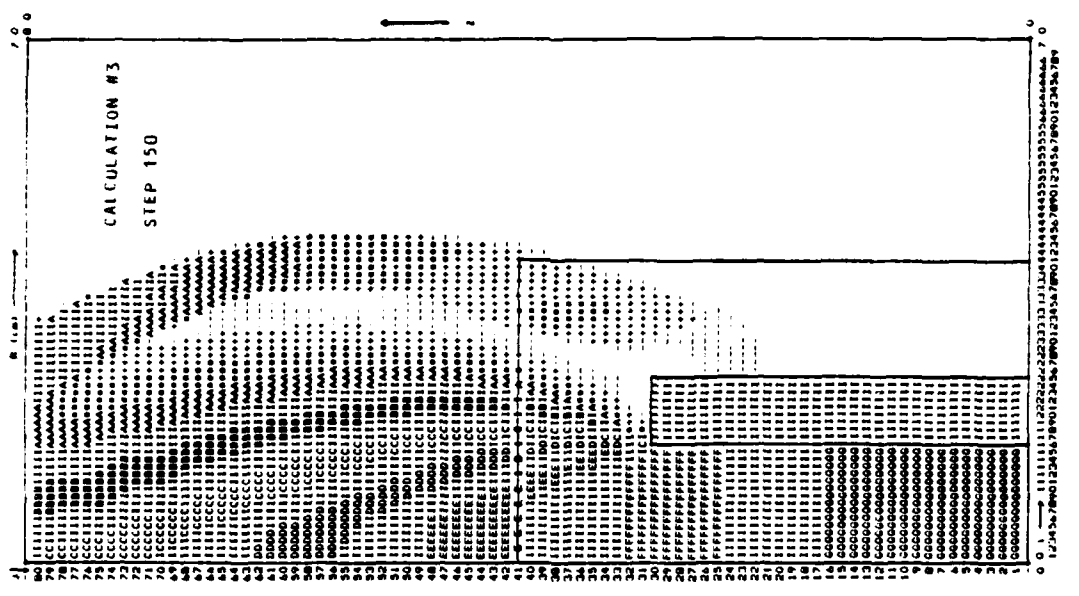


Figure 7. Step 150 for barrel Calculations #2, 3, and 4.

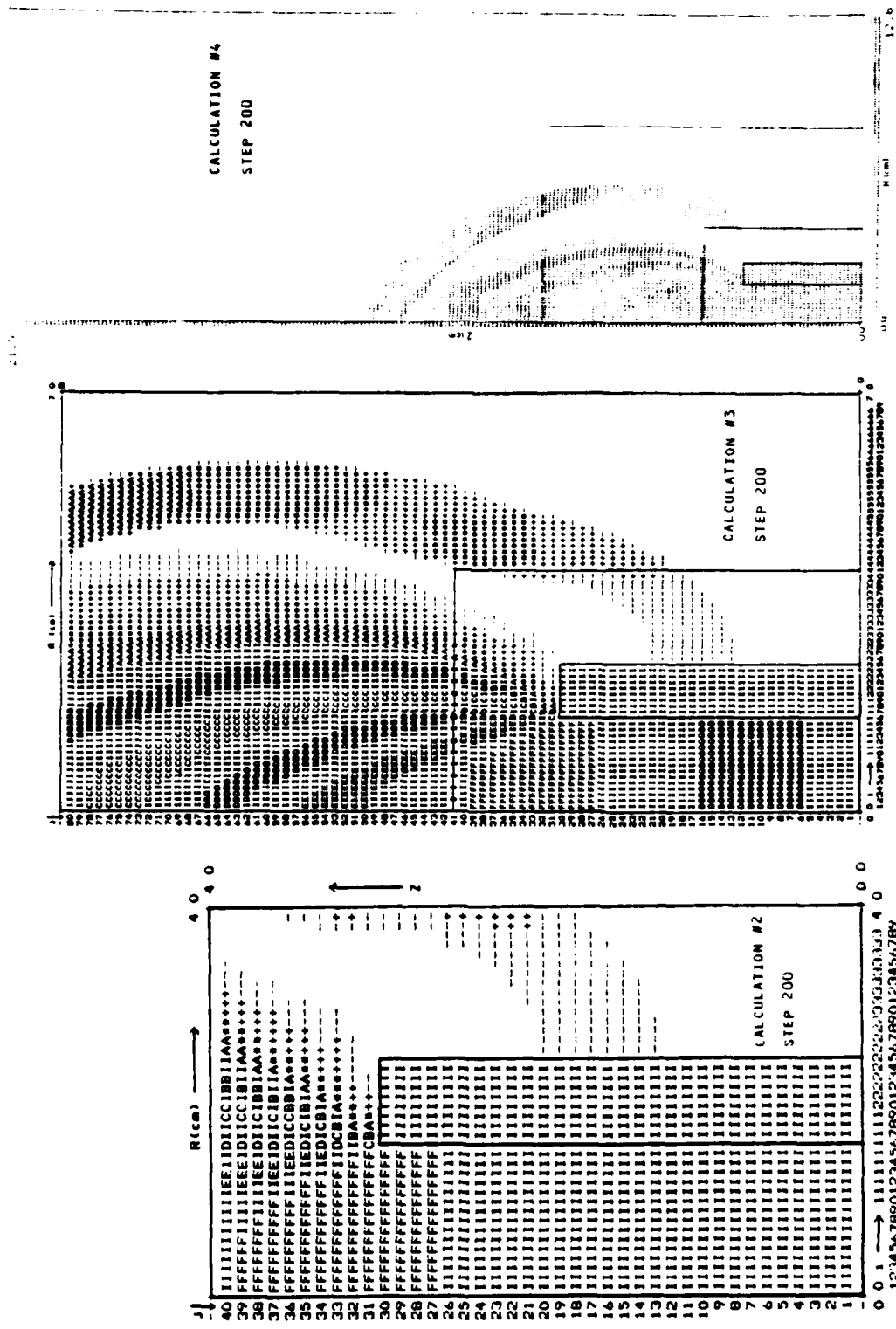


Figure 8. Step 200 for barrel Calculations #2, 3, and 4.

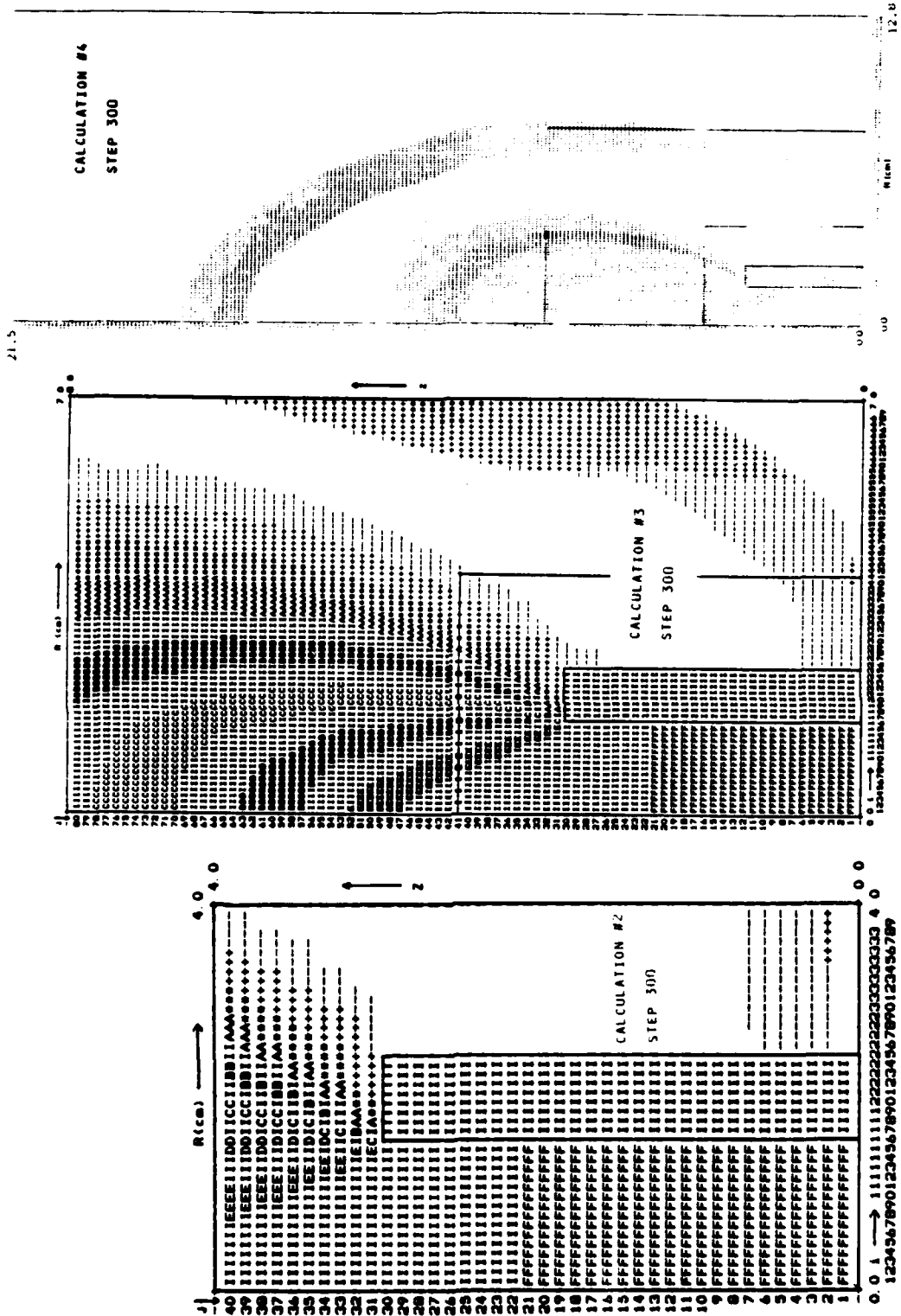


Figure 9. Step 300 for barrel Calculations #2, 3, and 4.

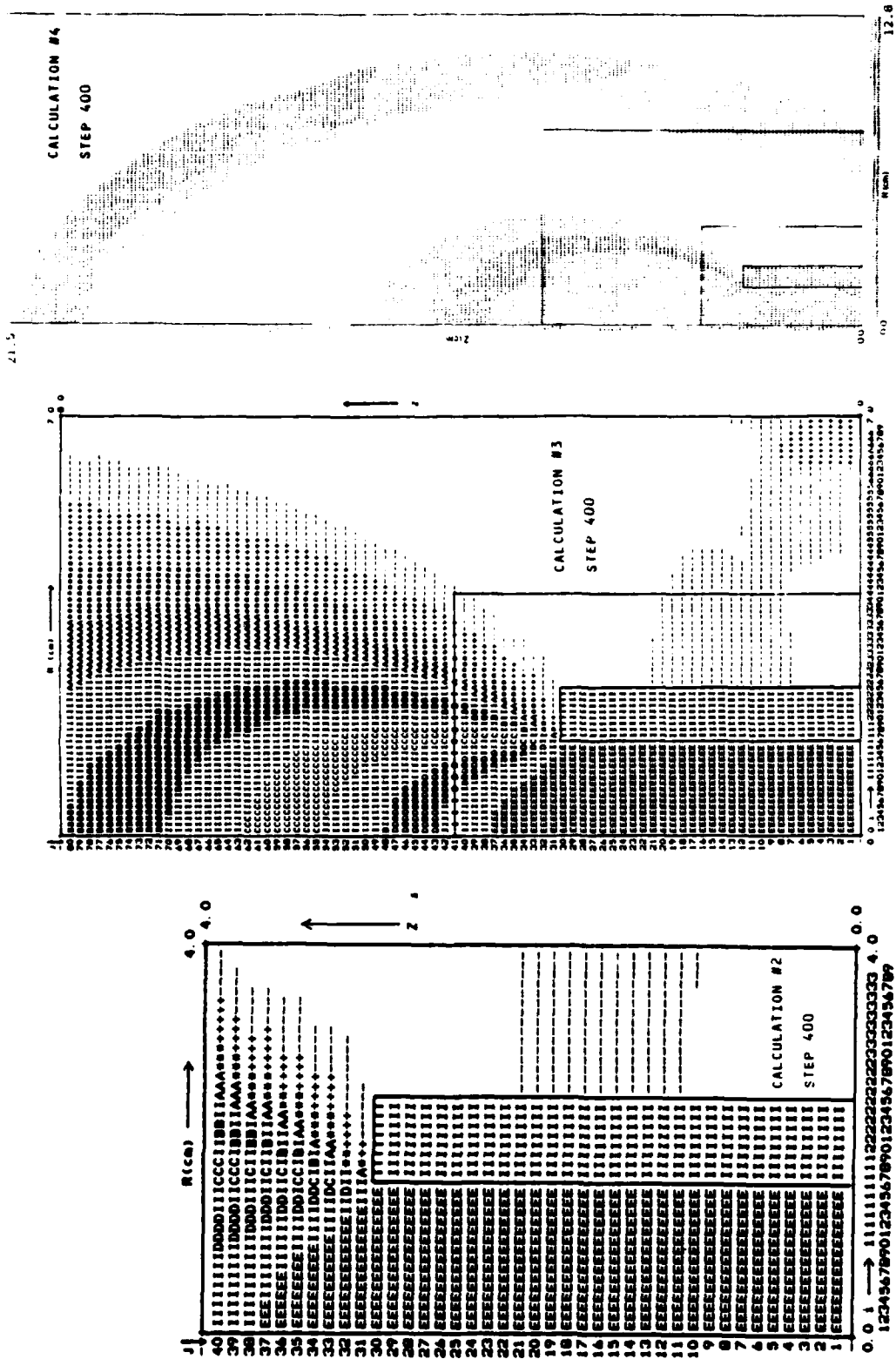


Figure 10. Step 400 for barrel Calculations #2, 3, and 4.

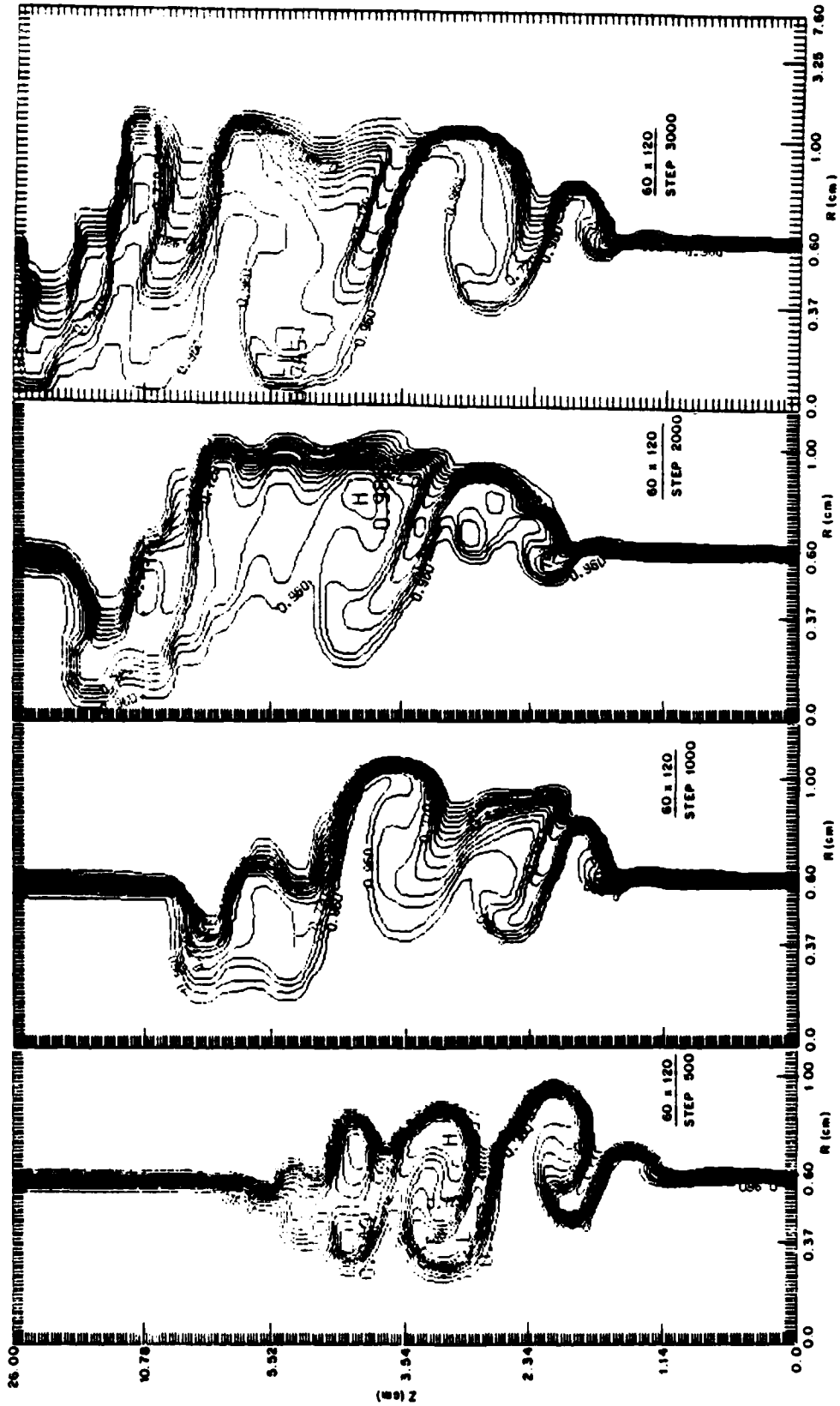


Figure 11. Contour plots of the mixing parameter R at four times in the cylindrical shear flow problem for the large 60×120 calculation.

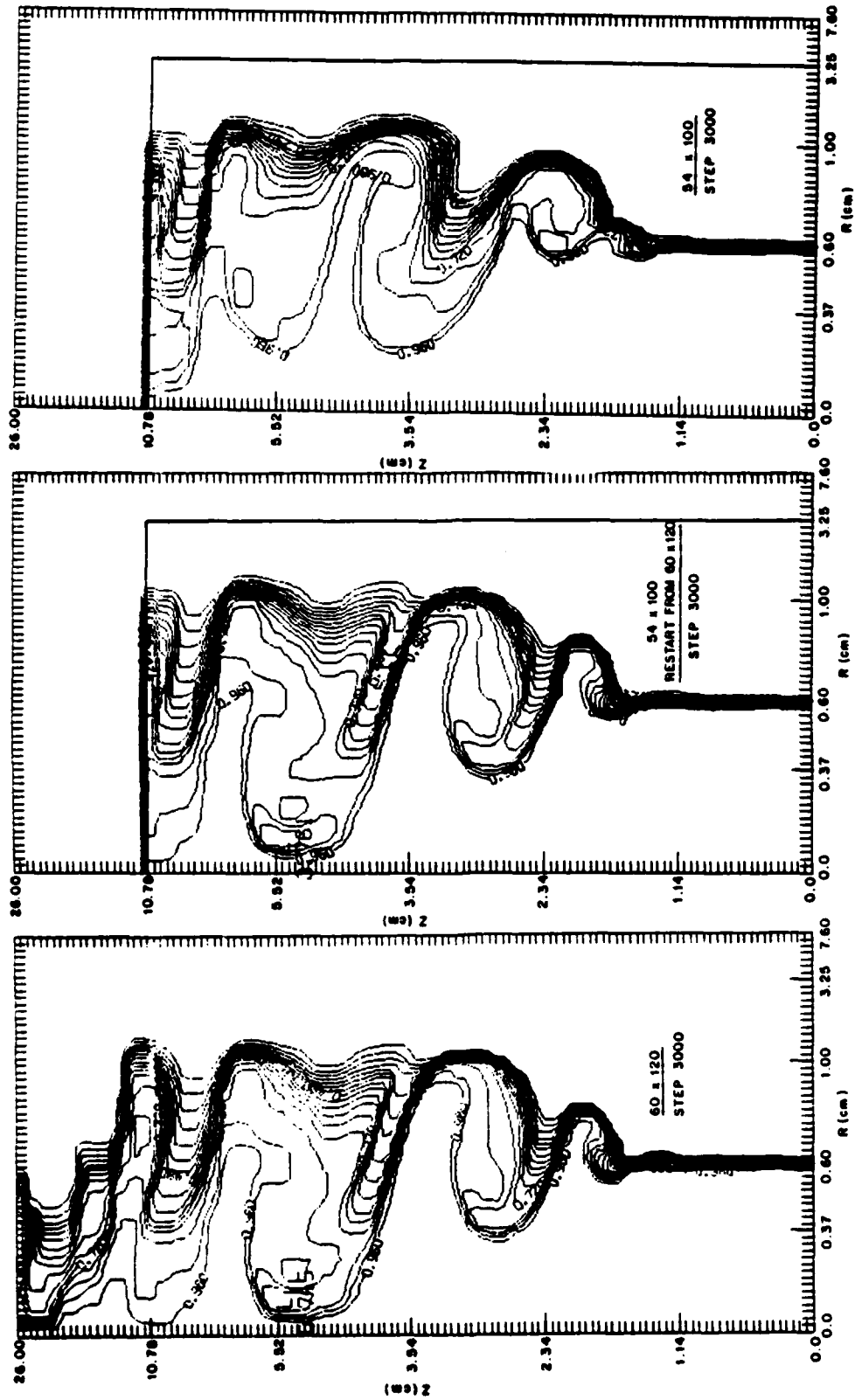


Figure 12. Comparison of contour plots of the mixing parameter R at step 300 for three calculations: 60 x 120, 54 x 100 restarted from the large calculation at step 2000, and a 54 x 100 calculation.

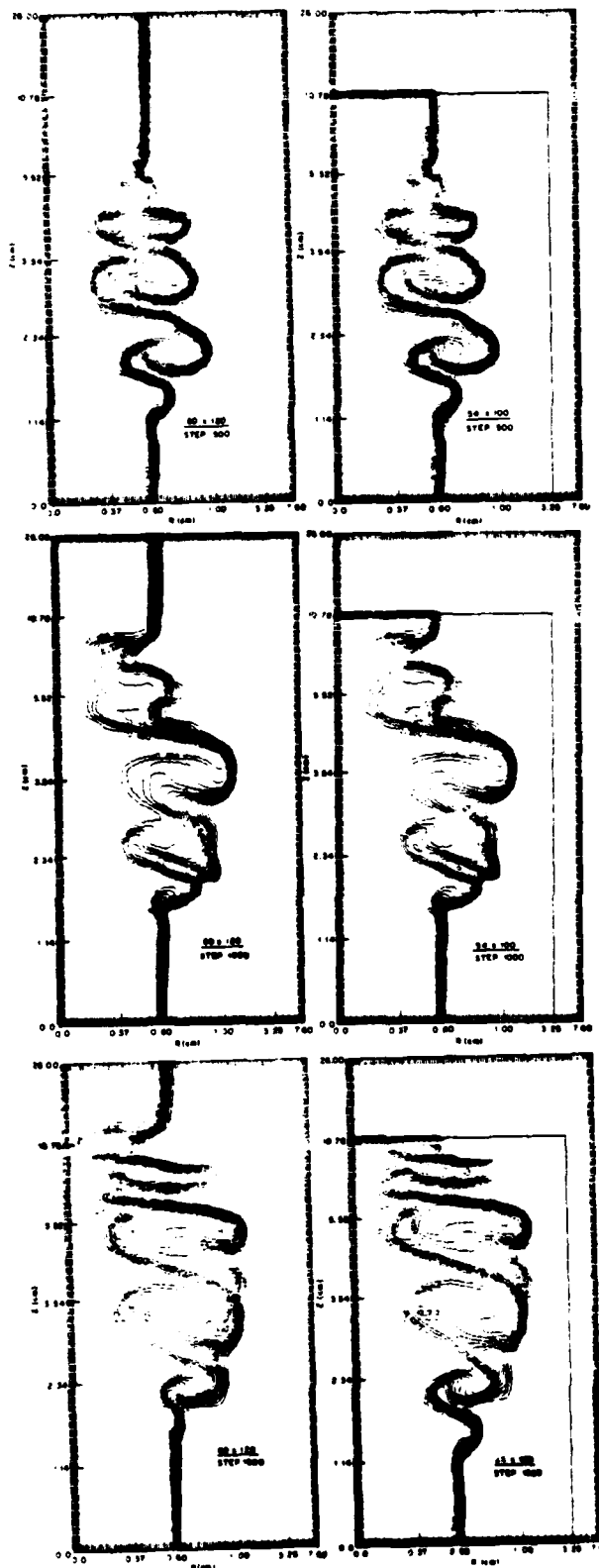


Figure 13. Comparison of the 60×120 and 54×100 calculations at three early times in the calculation.

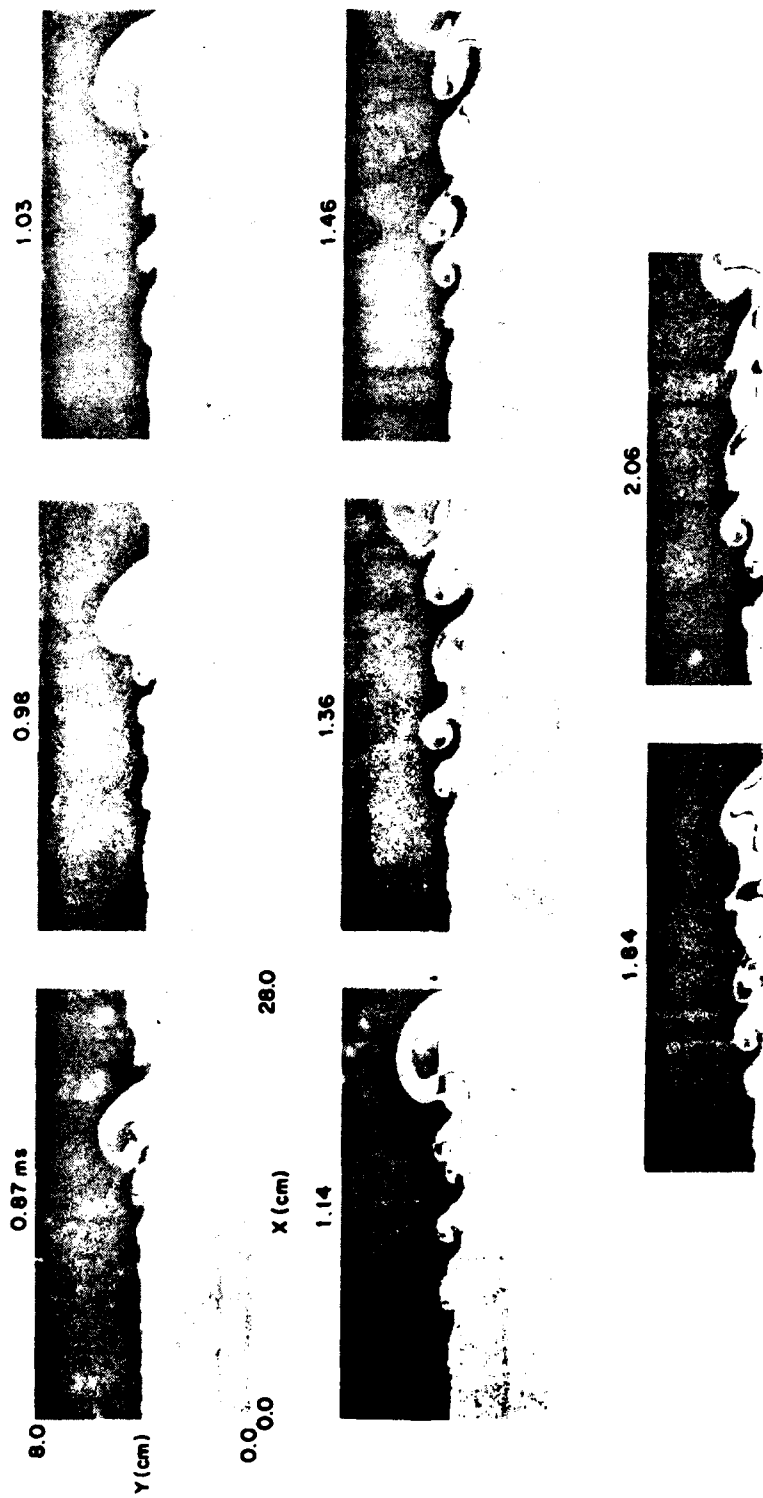


Figure 14. Flow plots of the mixing parameter P for the splitter plate experiment.

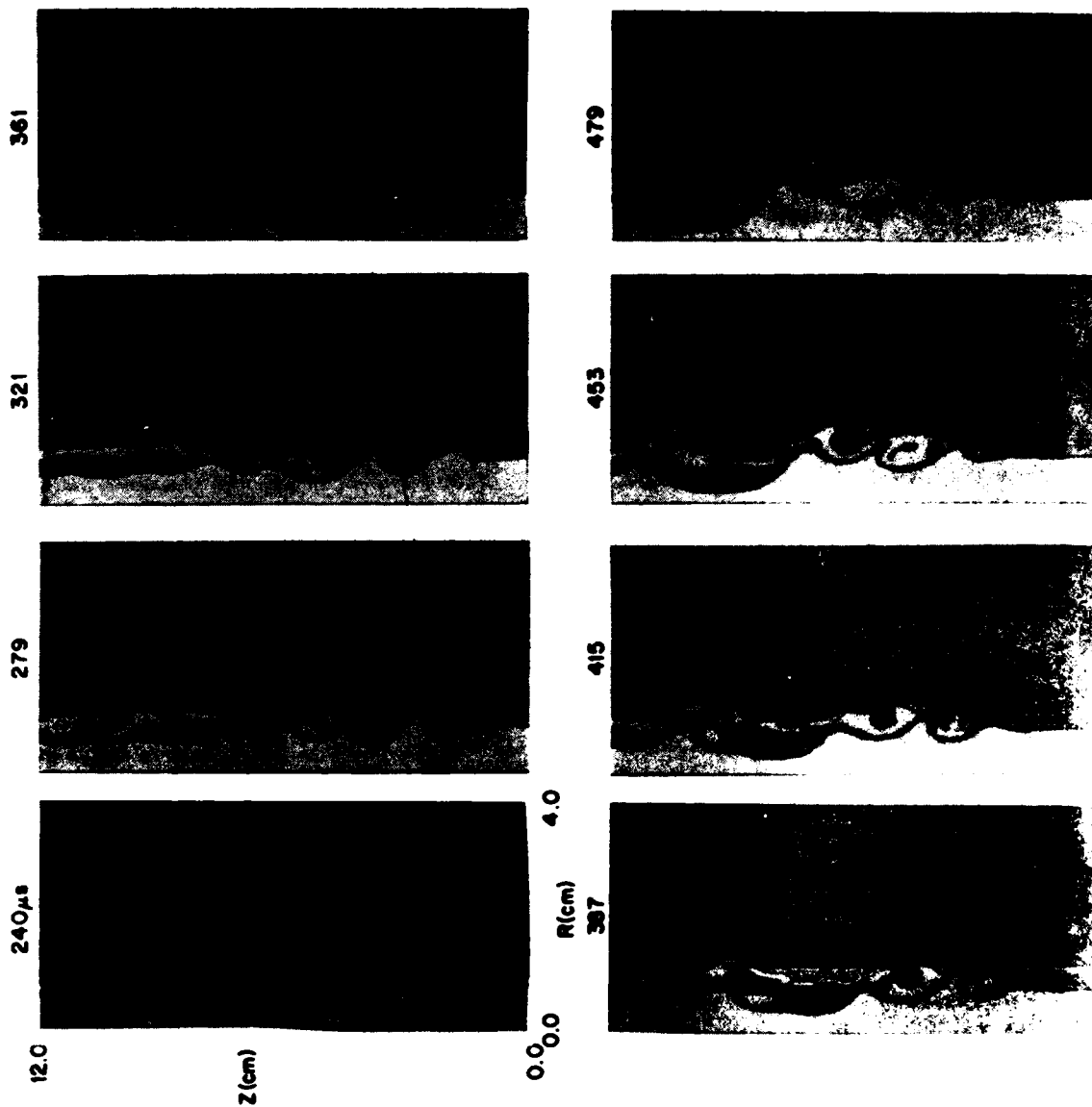


Figure 15. Shadow plots of the mixing parameter R for the calculation of a fast air jet moving into a slower coflowing air jet.

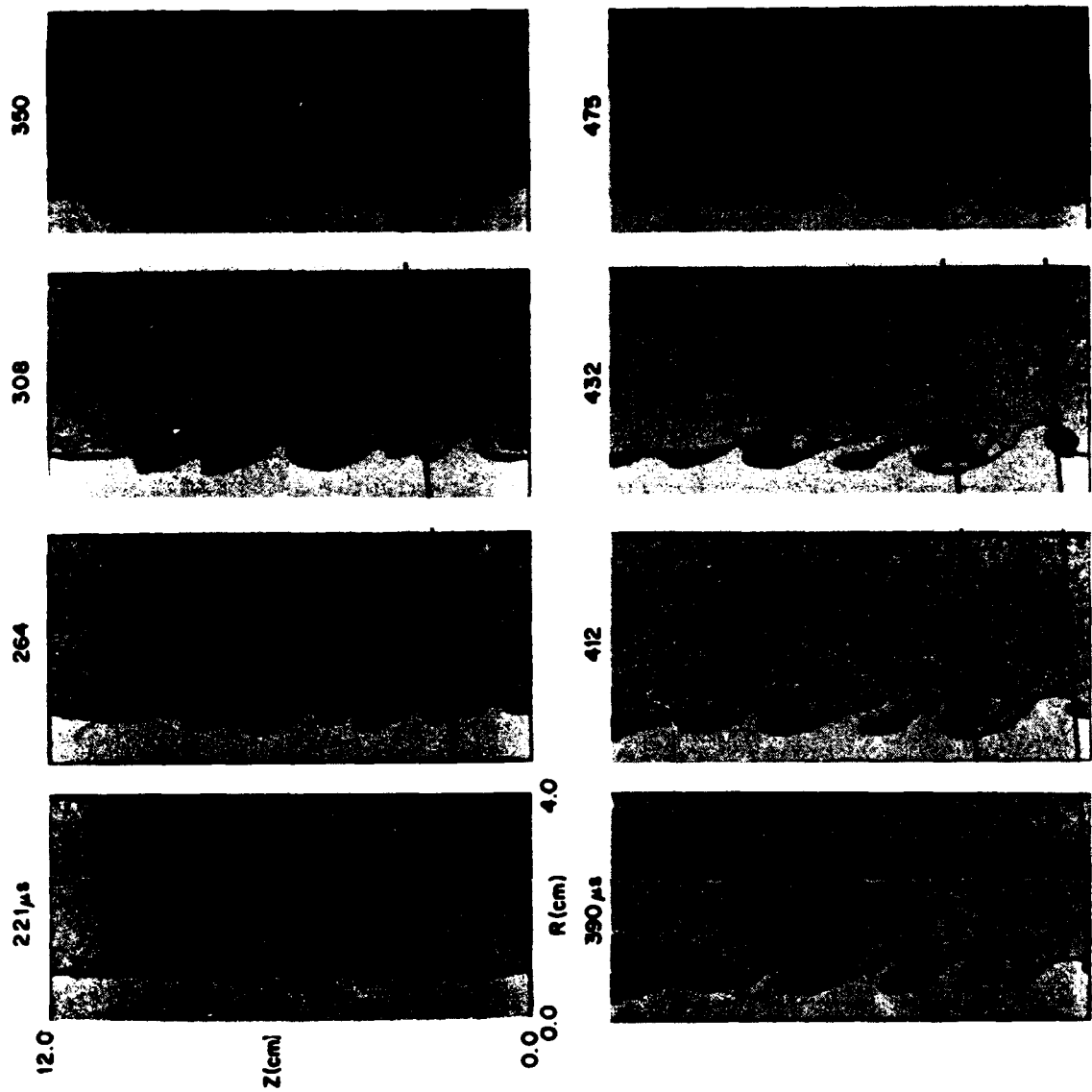


Figure 16. Shadow plots of the mixing parameter R for the calculation of a fast air jet moving into a slower coflowing freon jet.

REFERENCES

- Book, D., J. Boris, A. Kuhl, E. Oran, M. Picone, S. Zalesak (1980), Simulation of Complex Shock Reflections from Wedge in Inert and Reactive Gas Mixtures, Proceedings of the 7th International Conference on Numerical Methods in Fluid Dynamics, pp. 84-90, Springer-Verlag, New York.
- Boris, J.P. (1976a), Flux Corrected Transport Modules for Solving Generalized Continuity Equations, Naval Research Laboratory Memorandum Report 3237.
- Boris, J.P., (1976b) Numerical Solution of the Continuity Equation, Proceedings of the Second European Conference on Computational Physics, North Holland Pub. Co., 1976. Also, NRL Memorandum Report 3327, Naval Research Laboratory, Wash., D.C., 20375.
- Boris, J.P., and D.L. Book (1976), Solution of Continuity Equations by the Method of Flux Corrected Transport, in Methods in Computational Physics, Vol. 16, 85-129, Academic Press, New York.
- Browand, F.K., and P.D. Weidman (1976), Large Scales in the Developing Mixing-Layer, J. Fluid Mech., 76, 127-144.
- Browand, F.K., and C.D. Winant (1973), Laboratory Observations of Shear Layer Instability in a Stratified Fluid, Boundary-Layer Meteor., 5, 67.
- Brown, G., and A. Roshko (1974), On Density Effects and Large Structure in Turbulent Mixing Layers, J. Fluid Mech. 64, 775-816.
- Chigier, N.A., and A.J. Yule (1979), The Physical Structure of Turbulent Flames, AIAA Paper 79-0217, New York.
- Landau, L.D., and E.M. Lifshitz (1959), Fluid Mechanics, Pergamon Press, New York.
- Liepmann, H.W. (1979), The Rise and Fall of Ideas in Turbulence, American Scientist, 67, 221-228.
- Oran, E.S., and J.P. Boris, Detailed Modelling of Combustion System, Prog. Energy Combustion Sci. 7, 1, 1981.
- Oran, E.S., T.R. Young, J.P. Boris, J.M. Picone, D.H. Edwards (1982) Nineteenth Symposium (International) on Combustion, 1982, p. 573. The Combustion Institute, Pittsburgh.
- Overman, E.A., and N.J. Zabusky (1981), Transition, Interaction and Scattering of Euler Equation V-States via Contour Dynamics, Technical Report ICMA-81-29, Institute for Computational Mathematics and Applications, Department of Mathematics and Statistics, University of Pittsburgh, Pittsburgh, PA, 15261.

- Picone, J.M. and J.P. Boris (1983), Vorticity Generation by Asymmetric Energy Deposition in a Gaseous Medium, Phys. Fluids 26(2), 365-382.
- Roshko, A., (1976), Structure of Turbulent Shear Flows: A New Look, AIAA Journal 14, 1349-1357.
- Turkel, E. (1980), Numerical Methods for Large-Scale Time-Dependent Partial Differential Equations, in Computational Fluid Dynamics, pp.128-262 ed. W. Kollman, Hemisphere Press, Wash., D.C.
- Wynanski, I., and H. Fiedler (1970), The Two-Dimensional Mixing Region, J. Fluid Mech. 41, 327-361.
- Yule, A.J (1981) Investigations of Eddy Coherence in Jet Flows, in The Role of Coherent Structures in Modelling Turbulence and Mixing, ed. J. Jimenez, Springer-Verlag, New York.
- Zabusky, N.J. (1981), Computational Synergetics and Mathematical Innovation, J. Comp. Phys. 43, 195.

DTIC 88